

## Research Article

# Characterization of Nanoscale Pores in Tight Gas Sandstones Using Complex Techniques: A Case Study of a Linxing Tight Gas Sandstone Reservoir

Chaohui Lyu <sup>1,2</sup>, Liguang Zhong,<sup>1</sup> Zhengfu Ning,<sup>1</sup> Qing Wang <sup>1</sup> and David R. Cole<sup>2</sup>

<sup>1</sup>China University of Petroleum, Beijing, China

<sup>2</sup>School of Earth Sciences, The Ohio State University, Columbus, Ohio, USA

Correspondence should be addressed to Chaohui Lyu; lvchaohui521@163.com

Received 28 October 2021; Revised 24 November 2021; Accepted 4 December 2021; Published 27 December 2021

Academic Editor: Mohammed Fattah

Copyright © 2021 Chaohui Lyu et al. This is an open access article distributed under the Creative Commons Attribution License, which permits unrestricted use, distribution, and reproduction in any medium, provided the original work is properly cited.

Pore structures with rich nanopores and permeability in tight gas reservoirs are poorly understood up to date. Advanced techniques are needed to be employed to accurately characterize pore structures, especially tiny pores which include micron and nanopores. In this study, various experimental techniques such as scanning electron microscopy (SEM), nuclear magnetic resonance (NMR)  $T_2$ , nitrogen adsorption method, and NMR cryoporometry (NMRC) are combined to interrogate the complex pore systems of the tight gas reservoir in the Linxing formation, Ordos Basin, China. Results show that tight gas sandstones are primarily comprised of residual interparticle and clay-dominated pores. Clay and quartz are two dominant minerals while pyrite occupies a nontrivial amount as well. The permeability of tight gas sandstones is very low, exhibiting an extremely poor positive correlation with porosity. While pore types and relative pore contents are more influential factors on the permeability, accurate characterization of pore size distribution is critical for the permeability of tight gas sandstones. Therefore, complementary characterization methods are carried out, indicating that neither small pores with radii  $< 100$  nm (around peak 1 in NMR  $T_2$  distribution) nor large pores with radii  $> 5 \mu\text{m}$  (around peak 3 in NMR  $T_2$  distribution) control the permeability by analyzing the connectivity of the pores in various size ranges, but rather pores averaging approximately  $350 \pm X$  nm (around peak 2 in NMR  $T_2$  distribution) have sufficient connectivity to host and transmit hydrocarbons. The pore size of tight gas sandstones is dominated by the clay-rich mineral assemblage. The study shows that the NMRC technique can be a very promising method, especially when referred to as a promising “roadmap” on how to interrogate tight formations such as the tight gas sands or even shale especially for the nanopore characterization.

## 1. Introduction

With the gradual depletion of conventional oil and gas systems, unconventional reservoirs have become the focus of the energy market. Of these, a tight gas sandstone reservoir is an important member [1, 2]. The definition of a tight gas reservoir is “a reservoir that cannot be produced at economical flow rates nor recovery economic volumes of natural gas, unless the well is stimulated by a large hydraulic fracturing or produced by the use of a horizontal wellbore or multilateral wellbores” [3, 4]. In addition, low permeability reservoirs developed in the past are mostly sandstones.

Whether a gas reservoir qualifies as tight or not depends on both physical and economic factors, as with tight oil sandstones, tight gas is associated with low porosity ( $< 10\%$ ) and commonly extremely low permeability ( $< 0.1$  mD) reservoirs produce mainly dry natural gas—i.e., methane [5–7]. Tight gas sandstones are characterized by a wide pore-size range, poor connectivity, and significant heterogeneity [5, 8]. Four types of pores observed by SEM include residual interparticle pores, grain dissolution pores, intercrystalline pores, and small microcracks [9]. Zhu et al. concluded that the large pores in the sandstone samples are more complex, which is also one of the primary causes of the sample heterogeneity [2]. Xiao et al. classified pore

size of tight gas reservoirs into three scales: clay-associated pores and intraparticle dissolution pores are less than  $0.5\ \mu\text{m}$ , the narrow slits between grains and the quartz intercrystalline pores range  $0.5\text{--}1.5\ \mu\text{m}$ , and the interparticle-related pores are larger than  $1.5\ \mu\text{m}$  [10]. Lai et al. suggested that micropores and mesopores provide most of the pore volume, whose pore size is less than  $50\ \text{nm}$  [11]. According to Shi et al.'s results, almost half of the pore space is occupied by the clay and capillary bound water [12]. In short, pores with radii ranging around nanoscale are critical for the pore volume and permeability of tight gas sandstone.

Pore structures of tight sandstones control the flow capacity, water saturation, and the producible pore volume, which are key factors affecting the gas production. Lyu et al. and Huang et al. emphasized the importance of the pore throat size for the mobile fluid percentage of tight formations [13, 14]. Fluid bound to pores increases with the decrease in detrital quartz content and the increase in clay mineral content, whereas connected pores allowing mobile fluids increase with the increase in authigenic quartz content and the decrease in detrital quartz content [15]. The correlation of micropore ( $2.5\text{--}10\ \text{nm}$ ) abundance with porosity is altered by diagenesis and compaction, causing the weak correlations between porosity and permeability. Shao et al. concluded that large numbers of small pores contribute to high storage capacity, whereas small numbers of large pores improve the flow capability in tight formations [16]. However, Sakhae-Pour and Bryant demonstrated that samples exhibit greater production with an increased fraction of the intragranular porosity [17]. This is particularly true when the permeability is less than  $1\ \text{mD}$ , and the permeability is dominated by nanopores and micropores, following the size classification scheme by Loucks et al. [18]. Hence, nanopores are increasingly important for reservoir storage capabilities with decreasing permeability [9]. Based on the empirical permeability models, Kolodzie found that the permeability is best correlated with the throat size corresponding to a mercury saturation of  $35\%$  ( $r_{35}$ ), and Zhao et al. indicated that a throat radius corresponding to  $30\%$  mercury saturation ( $r_{30}$ ) is the dominant throat radius [19, 20]. Further, some researchers reported that pore throat radii corresponding to a mercury saturation of  $10\%$  ( $r_{10}$ ) are the best predictor of permeability for tight gas sands [21]. Permeability estimation models can be obtained by pore distribution and porosity. A part of pore types strongly affects coal permeability, including movable meso-macropore porosity and movable cleat porosity [22]. Different degrees of diagenesis and compaction cause various types of sandstones and determine the dominant pore size, which also emphasize the necessity for characterizing the variable pore types and sizes influencing porosity and permeability of tight gas sandstones [23].

In summary, previous studies emphasized the stronger relationship between permeability and pore sizes of tight reservoirs than that between permeability and the total porosity [24, 25]. Therefore, attentions should be paid to a comprehensive description of pore sizes and pore types (pore structures). However, detailed characterization of pore features in tight gas sandstones is less well documented in the literature. Various current techniques have been applied

to pore structure characterization of porous media, including fluid invasion methods (mercury injection porosimetry [13] and nitrogen adsorption method [26]), direct imaging methods (SEM, transmission electron microscopy) [27], and noninvasion methods (X-ray computed tomography, NMR) [28–30]. Among the techniques above, mercury injection porosimetry and nitrogen adsorption, along with SEM, can detect tiny pores. However, pore structures can be distorted by mercury injection porosimetry with high pressure, while ink-bottle pore throat structures are probably not well constrained [20, 31].

The focus of this study is to explore a new technique to probe small pore features and their size, shape, and connectivity because nanopores ( $<50\ \text{nm}$ ) comprise a nontrivial fraction of porosity in tight sandstones. NMRC is a fairly new method that has been gradually applied to many porous media, such as silica gel, cements, bones, and fibers [32–34]. For example, Hansen et al. reported highly consistent results between pore size distributions of industrial silica, determined by nitrogen adsorption isotherm and NMRC methods. Cement and cement paste were widely tested by the NMRC method. The experimental results of Korb et al. showed that pore sizes ranging from  $2\ \text{nm}$  to  $500\ \text{nm}$  can be measured by NMRC precisely and reproducibly [35]. Pores with a radius of  $2\ \text{nm}$  were identified in bones by Gun'ko et al. using NMRC, and also, a large fraction of pore volume with pore sizes in the mesopore range was indicated in bone by NMR [36, 37]. Recently, NMRC has been utilized by the petroleum industry to characterize pore structure [38–40]. Z. P. Wang and T. Wang concluded that the pore information determined from NMRC demonstrated its advantage compared to other methods, with the ability to identify closed as well as open micropores accurately below  $20\ \text{nm}$  [41]. A number of studies on petroleum reservoir samples found that the NMRC method produced results consistent with the mercury intrusion method or the nitrogen adsorption curve, especially for shale and coal [38, 42, 43]. The NMRC results of shale powder reflect the information on not only open pores but also closed ones [42]. In addition, NMRC usually yields larger pore volume than the nitrogen adsorption method, since drying for BET analysis induces pore shrinkage/collapse [38]. However, as noted previously, few studies have been done on tight gas sandstones using NMRC.

The purpose of this study is to explore the application of NMRC on tight gas sandstone samples with different magnitudes of permeability collected from Linxing tight gas sandstone reservoirs, China. The focus is on the pore structures, especially nanopores and their influences on permeability. NMR  $T_2$  was employed to obtain the full pore size distribution and also used to obtain the pore morphology when in concert with SEM. NMRC and nitrogen adsorption method were used to characterize pores with small size. The ultimate aim of the study is to explore the application of NMRC to nanopores of tight gas sandstones and obtain more detailed and accurate information of pore structures.

## 2. Experiment Section

*2.1. Samples.* The Linxing area is mainly located in the eastern edge of the Ordos Basin, China, and the structure is

located around the Yishan slope, Ordos Basin, and Shanxi western flexure belt. Core samples (Figure 1) were collected between 1923 and 1929 meters depth of the LX-35 Well, Taiyuan Group, which belongs to tight gas sandstones. Table 1 indicates that the permeability of these low-porosity samples decreases with the increase in depth, from 0.88 mD to 0.05 mD. Contact angle results in Table 1 show a strong water wettability, which is related to the high clay content as shown in Table 2. X-ray results show that clay plus quartz exceeds 95% of the total mineral content, each exceeding 44%. Sample LX1 contains 3.2% pyrite, while minor feldspars also appear in samples, including K-feldspar and plagioclase.

In addition, the sample was divided into two parts: one part is for the NMR  $T_2$  test and the other part is prepared for three separated assessments. Tight sandstone powder is for nitrogen adsorption, a tight sandstone fragment is for NMRC, and a tight sandstone slice is for SEM.

**2.2. NMRC Setup.** The sketch in Figure 2 is NMRC12-010V from Suzhou Niumag Analytical Instrument Corporation. The setup is mainly composed of two systems: a temperature controlling system and an NMR system. The instrument has a resonance frequency of 11.537 MHz, a magnet temperature controlled around  $32.00 \pm 0.02^\circ\text{C}$ , and a probe coil diameter of 10 mm. The temperature range is  $-35^\circ\text{C}$  to  $40^\circ\text{C}$  ( $-308 \sim 233$  K) with an accuracy of  $\pm 0.1^\circ\text{C}$ .

**2.3. Experimental Procedure.** Nitrogen adsorption-desorption isotherm measurement has been frequently described in publications [4, 42]. Hence, the experiment procedure is not discussed in our manuscript. The experimental parameters and procedures of NMR  $T_2$  and NMRC procedures are introduced as follows.

**2.3.1. NMR  $T_2$  Measurement.** The procedures are described as follows. First, dry weight and core size (length, diameter) of the samples are measured. Second, samples are evacuated for 2 hours and then saturated with distilled water under 25 MPa for 48 hours. After the saturation, wet weights are measured. The water porosity of each core is calculated by dry weight, wet weight, and its volume. Third, raw NMR data of water-saturated cores are performed. The NMR CPMG parameters are listed as follows: echo spacing, 0.1 ms; waiting time, 300 ms; echo numbers, 6000; and numbers of scans, 32.

**2.3.2. NMRC Measurement.** As a comparison, the samples for NMRC are cut from NMR  $T_2$  samples with the length of  $\sim 0.5$  cm. Detailed experimental procedures are as follows: step (1): fragment samples were evacuated for 8 hours and then saturated with distilled water for 48 hours (20 MPa); step (2): NMR tubes filled with samples were inserted into the middle of the probe coil; and step (3): the temperature system lowered the sample temperature to  $-30^\circ\text{C}$  to freeze all fluids in pores and then increased it to  $10^\circ\text{C}$  at  $0.1^\circ\text{C}$  increments. At the same time, the fluid content was detected by NMR CPMG spin echo sequencing as a function of changing temperature. The NMR CPMG parameters are



FIGURE 1: Three tight gas sandstone cores from Linxing area, Taiyuan Group, Ordos Basin.

TABLE 1: Petrophysical properties of the three tight gas samples.

Core	Depth (m)	Diameter (cm)	Porosity (%)	Gas permeability (mD)	Contact angle ( $^\circ$ )
LX1	1929	2.53	3.3	0.05	11.03
LX2	1924	2.53	3.8	0.21	9.92
LX3	1923	2.53	4.4	0.88	18.26

listed as follows: echo spacing, 0.1 ms; waiting time, 500 ms; echo numbers, 2500; and numbers of scans, 128.

**2.4. NMRC Principles.** During the NMRC measurement, porous media are saturated with a fluid, cooled to a base temperature, and then heated at increments of  $0.1^\circ\text{C}$ . The phase change of fluids in pores with temperature follows the Gibbs-Thomson equation (equation (1)) [44, 45].

$$\Delta T_m(x) = T_m^\infty - T_m(x) = \frac{4\sigma_{sl}T_m^\infty}{x\Delta H_f\rho_s}, \quad (1)$$

where  $x$  is the crystal diameter, since the pore is filled with the fluid or crystal; thus,  $x$  also represents the diameter of the pore;  $T_m(x)$  is the melting point of crystal with diameter of  $x$ ;  $T_m^\infty$  is the melting point of the crystal with infinite diameter;  $\sigma_{sl}$  is the surface energy at the crystal-liquid interface;  $\rho_s$  is the solid density;  $\theta$  is the contact angle between fluid and pore surface; and  $\Delta H_f$  represents the bulk enthalpy of fusion (per gram of material). Equation (1) can be simplified to

$$\Delta T_m(x) = \frac{k_g \cdot k_s \cdot k_i}{x}, \quad (2)$$

where  $k_g$  is the geometric constant,  $k_s = \sigma_{sl}/\Delta H_f\rho_s$ ,  $k_s$  is a constant related to the solid-fluid system, and  $k_i$  is a constant related to surface energy and reflects the contact angle between fluid and pore wall.  $\Delta T_m(x)$  is the melting point depression.

TABLE 2: Mineral contents of tight gas sandstones (wt.%).

Sample	Quartz	K-feldspar	Plagioclase	Siderite	Pyrite	Iron-dolomite	Clay
LX1	45.6	1.1	—	—	3.2	—	50.1
LX2	54.9	—	—	—	—	—	45.1
LX3	44.6	0.8	0.8	2.5	—	1.0	50.4

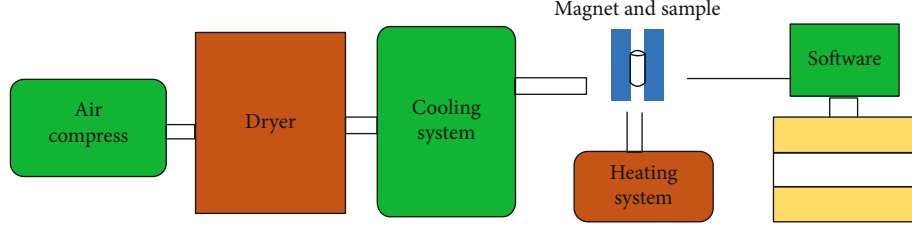


FIGURE 2: The sketch of the NMR cryoporometry analysis system.

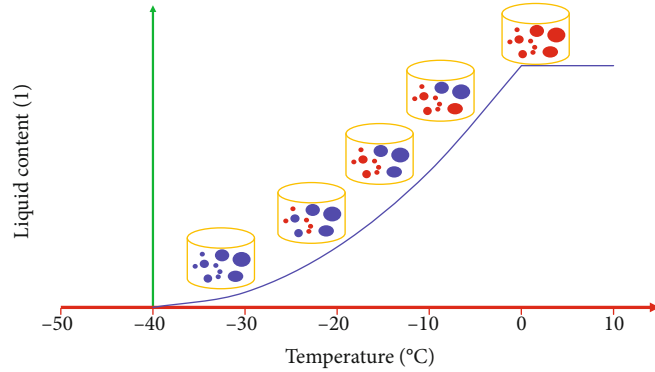


FIGURE 3: Melting point curve and phase transition behavior of water in porous materials (blue ball means solid; red ball means fluid).

$$\Delta T_m(x) = \frac{k_{GT}}{x}. \quad (3)$$

The product of  $k_g$ ,  $k_s$ , and  $k_i$  can be represented by  $k_{GT}$ , which is the thermodynamic constant. The value of  $k_{GT}$  is 58 (with the unit of  $K \cdot nm$ ) for distilled water when used to convert the melting curves.

From equation (3), the pore size has the one-to-one relationship with the melting point depression [46]. The process of increasing the total fluid content with increasing temperature can be regarded as a progressive accumulation process of pore volume from small pores to large ones, in which the fluid volume can be measured by the probe (Figure 3). The relationship between fluid content and temperature in the process can be represented by either solidification or melting curves. Instead of tracking the solidification curve, the melting curve is selected as it yields greater reproducibility, which can be transferred to pore size distribution by the Gibbs-Thomson equation (equation (1)). Pores with radii ranging from 1 nm to 500 nm can be accurately measured by the NMRC method within the temperature range of  $-30^\circ\text{C}$  to  $0^\circ\text{C}$  ( $\pm 0.1^\circ\text{C}$ ). In addition, water wettability is a favorable situation for the accuracy of NMRC results when using distilled water as the filling fluid.

### 3. Results

**3.1. Pore Types and Minerals.** A TESCAN-VEGA SEM was employed to document the microscopic morphology, and the results are shown in Figure 4. Figures 4(a) and 4(d) show a full microscopic view of sandstone, which reveals most interparticle pores ranging between 1 and 5 microns.

Pores are filled with various minerals, including irregular platy kaolinite (Figure 4(f)), thick platy dickite (Figure 4(i)), and filamentous or flaky illite (Figures 4(h) and 4(i)). Clay-dominated pores are distributed in filamentous and platy illite and range between 1 and 4 microns (Figures 4(c) and 4(h)). Although pyrite was only detected in sample LX1 by X-ray, it can be observed by SEM in all three samples (Figures 4(b), 4(e), and 4(g)). As can be seen from Figure 4, residual interparticle pores and clay-dominated pores are the main pore types observed in tight gas formation. SEM observations indicate that microfractures are in low abundance, which differs from what others have seen in tight oil sandstones [13].

**3.2. NMR  $T_2$  Distributions at Full Saturation.** As can be seen from Figure 5, NMR  $T_2$  distributions of three tight gas sandstone samples all show three peaks, marked as P1, P2, and P3. Three peaks, respectively, range around 0.3 ms, 10 ms,

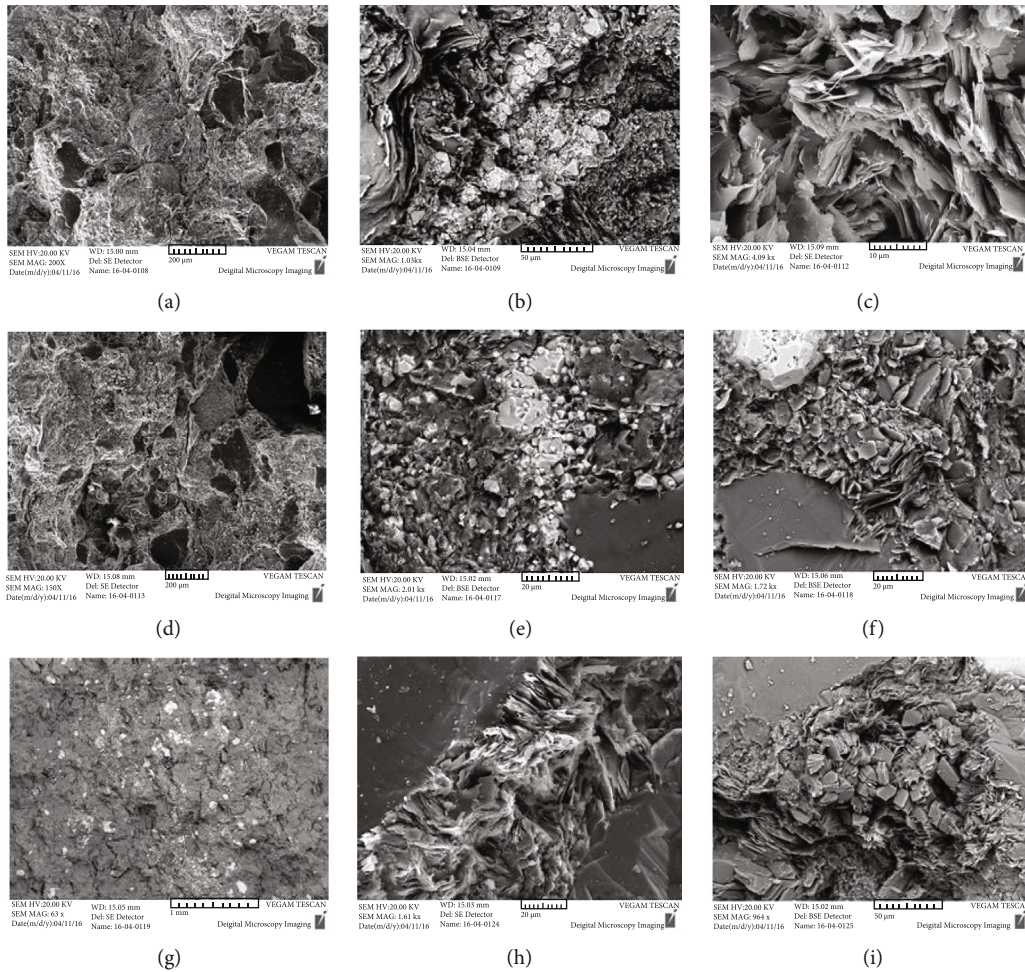


FIGURE 4: SEM results of three tight gas sandstone samples: (a) full microscopic view of tight gas, interparticle pores ranging 1-5 microns (LX3); (b) different stages of pyrite aggregation and platy biotite (LX3); (c) platy and filamentous illite with pore ranging around 1-3 microns (LX3); (d) full microscopic view of tight gas, interparticle pores ranging around 1-5 microns and poor connectivity (LX1); (e) different stages of pyrite distributed on the surface of the particles (LX1); (f) platy kaolinite filling interparticle pore (LX1); (g) full microscopic view of tight gas with rich white pyrite (LX2); (h) platy illite filling interparticle pores and forming 2-4 micron pores (LX2); (i) thick platy dickite and filamentous illite filling interparticle pores (LX2).

300 ms, respectively, except peak P3 of core LX3 distributed around 100 ms. Areas under P1 or P2 are both larger than that of P3 for all three samples, respectively, corresponding to three scales of pore size. Therefore, small pores are enriched developed in tight gas sandstones. The increase in peak intensities for P2 and P3 correlates with larger pores and increasing permeability.

The values of NMR  $T_2$  spectra have one-to-one relationship with pore radii. Three samples share a similar size range of small pores represented by P1 and P2, whereas pores represented by P3 for LX3 exhibit a smaller size compared to samples LX1 and LX2. In addition, three peak amplitudes of LX3 are greater than those of cores LX1 and LX2, indicating greater porosity and hence greater capacity to host fluids. Peaks P2 and P3 of LX3 are well connected, while two peaks of other two samples are disconnected. Because the permeability and porosity of LX3 are both larger than those of LX1 and LX2, as listed in Table 1, we suggest that the contradiction may be explained by the differences in connectivity

between peak P2 and peak P3. Peak P2 and peak P3 of LX3 are connected, indicating that pores are well connected.

**3.3. Nitrogen Adsorption-Desorption Isotherms.** Nitrogen adsorption-desorption isotherms of three samples belong to type IV of IUPAC definition [47]. As shown in Figure 6, the presence of mesopores (2-50 nm) is mainly reflected. Three adsorption isotherms start at the relative pressure value of 0.02, reflecting the presence of micropores (<2 nm). Because of capillary condensation or micropore filling during the adsorption, two isotherms do not coincide with the desorption curve located above the adsorption curve, which always forms a hysteresis or lag loop at high relative pressure, referred to as adsorption equilibrium isotherm of type IV. The characterization of lag loops reflects the distinct pore structure of tight gas sandstones [47, 48].

According to the IUPAC method, lag loops of three samples belong to the H3 type, in which the adsorption and desorption isotherms slowly rise; then, the amount of

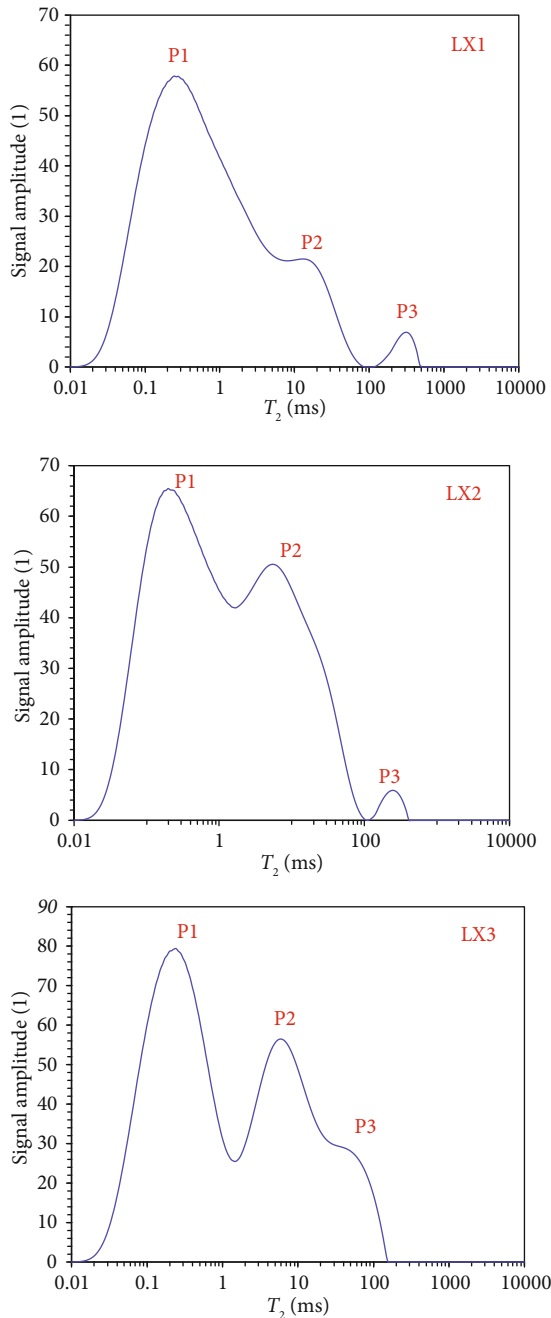


FIGURE 5: NMR  $T_2$  distributions of the three water-saturated samples.

adsorption increases rapidly at higher pressure and the desorption loops are initially narrower. These characteristics of adsorption and desorption isotherms reflect mesopores and may be caused by stacking platy particles. These pores are mainly slit pores. Based on the SEM results of Section 3.1, these platy minerals are probably illite, kaolinite, and dickite (Figures 4(c), 4(f), 4(h), and 4(i)).

Pore size distributions were also obtained using the BJH (Barrett-Joyner-Halenda) method, especially for micropores (2-50 nm). Figure 7 shows pore volumes of LX2 and LX3 evenly distributed between 2 and 100 nm, while that of LX1 ranges between 20 and 110 nm. The shape of curves of pore

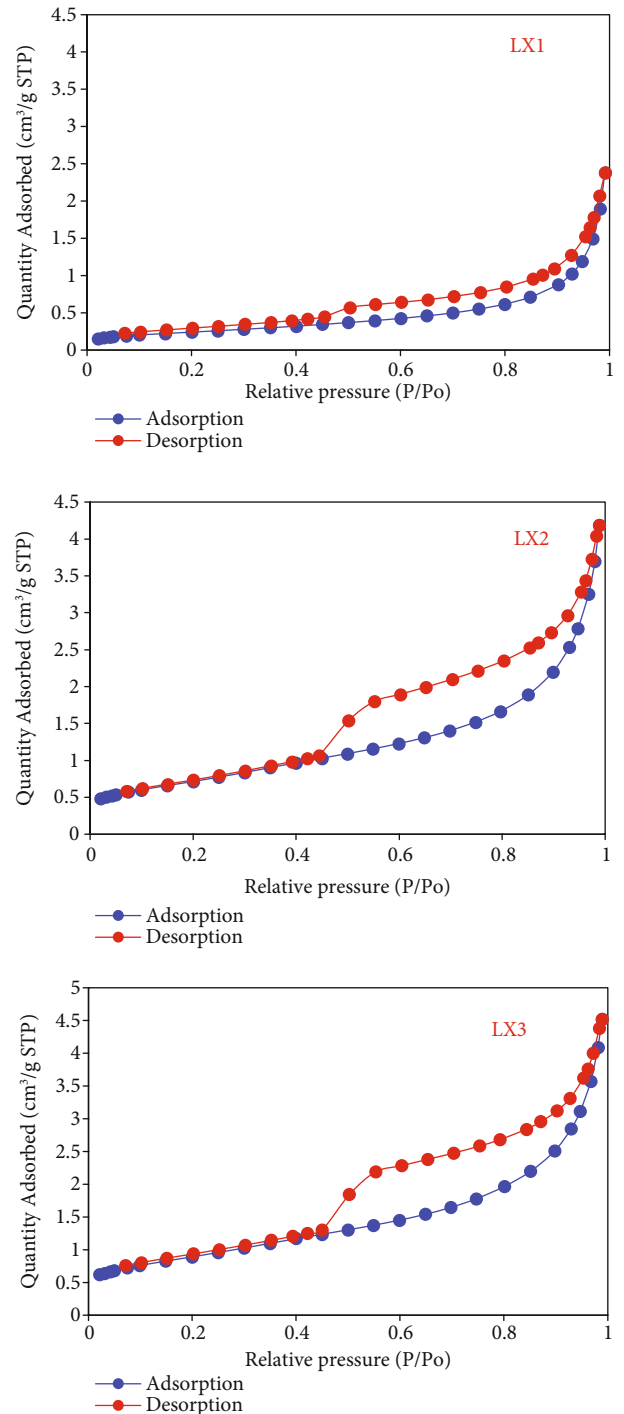


FIGURE 6: Nitrogen adsorption-desorption isotherms of the three samples.

volume versus pore sizes for three samples is very similar for pore sizes greater than 70 nm. As noted above, the biggest difference in pore development falls in the 2-30 nm range wherein LX2 and LX3 differ significantly from LX1.

**3.4. NMRC Results.** NMRC can directly obtain the pore volume versus pore size curves according to the linear relationship between pore volume and signal intensity.

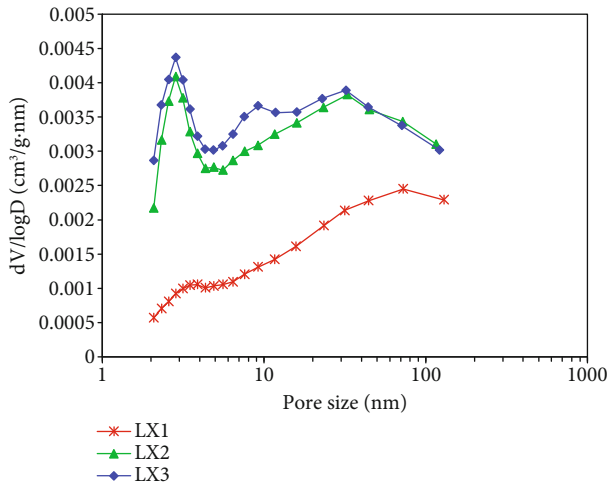


FIGURE 7: Pore size distribution of the three tight gas samples by nitrogen adsorption based on the BJH method.

Figure 8 shows the pore size (radius) distributions of three samples by NMRC, in the form of multiple peaks across a pore diameter range of 2 nm to 500 nm. The main pore volumes for three samples display somewhat different patterns in Figure 8; LX1 exhibits peaks distributed between 1 and 100 nm, and LX2 and LX3 have peaks ranging between 2 and 500 nm. The first five peaks of LX1 and LX2 are all located around 2 nm, 4 nm, 8 nm, 16 nm, and 65 nm, respectively. Pores of LX1 and LX2 distributed at 2 nm show the largest pore volume compared to pores observed at the other peaks, whereas seven peaks of LX3 are evenly spread from 2 nm to 500 nm. Similar to the results of nitrogen adsorption, pore volume versus pore size curves of LX2 and LX3 exhibit somewhat greater pore volume compared to LX1, but all three samples display similar peak positions especially for LX1 and LX2 apart from pores ranging around 1-2 nm. Pore volumes of nanopores (pore with radii  $< 2$  nm) of LX1 tend to be dominant, while pore volumes of micropores (pore with radii ranging 2-50 nm) and mesopores (pore with radii  $> 50$  nm) of LX2 and LX3 are more prominent compared to LX1 [49]. In summary, the pore volume of LX1 is mainly contributed by nanopores, whereas pore volumes of LX2 and LX3 are mainly contributed by micropores and mesopores.

## 4. Discussion

**4.1. Application of Three Methods to Nanoscale Pore Characterization of Tight Gas Sandstones.** NMRC, nitrogen adsorption, and NMR  $T_2$  were employed to characterize the pore structure of tight gas sandstones. NMR  $T_2$  distribution at full saturation can reflect the full pore size distribution of porous media. However, the conversion factor between NMR  $T_2$  and pore radii is difficult to determine. Radii of pores described by nitrogen adsorption ranged from one nanometer to tens of nanometers, while NMRC can describe pores with radii ranging from 2 nm to 500 nm. A comparison of results from nitrogen adsorption and NMRC is shown in Figures 7 and 8, respectively, indicating that pore

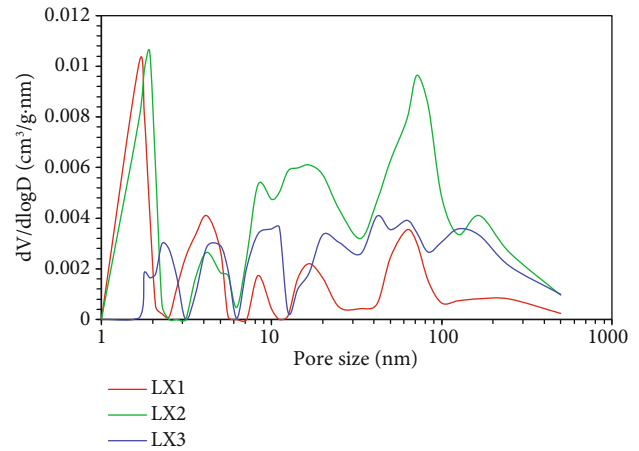


FIGURE 8: Pore size distributions of the three samples by NMRC.

size distributions determined by NMRC exhibit higher pore volumes relative to those from nitrogen adsorption. Hence, NMRC has a practical application to tight gas sandstones, especially for the nanopore characterization.

**4.2. Permeability, Porosity, and Pore Size Distribution.** Based on the results of three samples from the NMR  $T_2$  method,  $T_2$  values of main peaks are lower than 100 ms, and half of the total  $T_2$  signal is composed of the signal from water saturating small pores. The overall NMR  $T_2$  peak distributions reflect an increased relative pore volume with increasing permeability, as well as the total pore volume. However, P3 of LX1 and LX2 is located between 100-500 ms, while P3 of LX3 is located approximately between 50-200 ms. This indicates that LX1 and LX2 have wider pore size distributions than LX3. Pores associated with P3 of LX3 are smaller size than those of LX1 and LX2, whereas the pore connectivity of LX3 is greater than that of the other two samples. On one hand, the differences in connectivity among three samples may explain the variability in the permeability and pore size. Conversely, pores reflected by P1 are abundant but small, versus pores represented by P3 that are larger but rare. Therefore, we surmise that pores associated with the peak P2 ( $\sim 7$  ms) likely control the permeability. Based on our previous work and related studies [13], the conversion between NMR  $T_2$  and pore size for tight sandstone formations is about 50 nm/ms, where pores associated with P2 are about 350 nm. The combination of Nitrogen adsorption and NMRC provide a solid basis for characterizing these pores accurately across roughly two orders of magnitude in dimension.

The pattern of pore size distribution curves determined by NMRC shown in Figure 8 does not coincide with the sequence of permeability values. Based on the weighted mean calculation of NMRC pore sizes, the results of the weighted mean pore diameters are 25.8 nm, 41.31 nm, and 49.99 nm, respectively, for LX1, LX2, and LX3. These values of the weighted pore diameters are consistent with the sequence of permeability values. Because pores with radii ranging 1-10 nm exhibited by LX1 and LX2 are abundant, it results in a low relative proportion of larger pores as well as the poorer connectivity. Three tight gas samples share

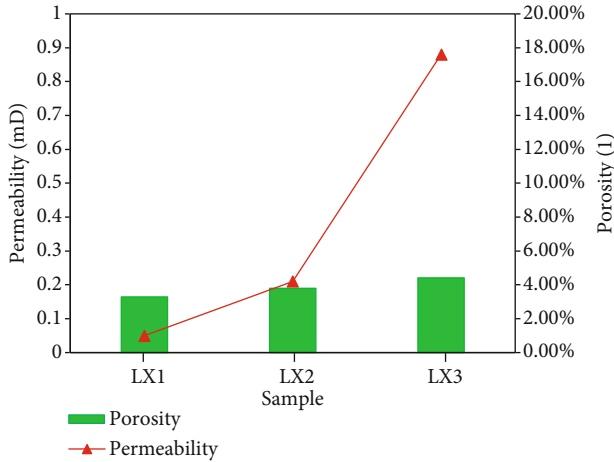


FIGURE 9: Permeability and porosity of the three samples.

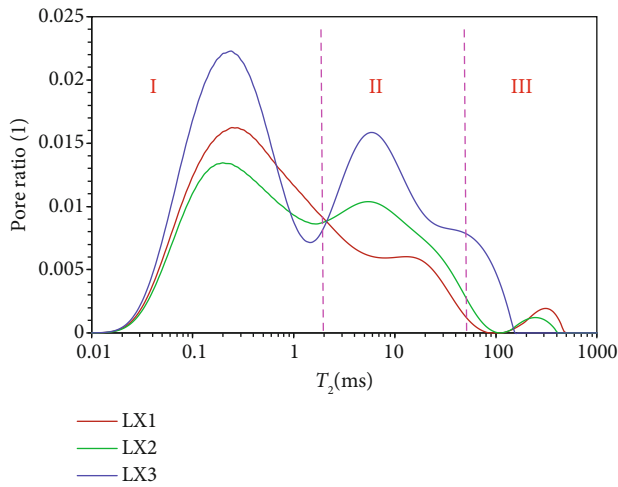


FIGURE 10: Pore size ratio distribution of the three tight gas sandstone samples.

almost the same porosity and mineral composition but very different permeabilities. Figure 9 indicates that the correlation between permeability and porosity is weak. The significant difference in permeability probably reflects differences in the relative ratios of pore size to pore throat diameters. The pore size can be divided into three intervals, which is marked in Figure 10. The sequence of pores falls in NMR  $T_2$  interval II of the pore size distribution in Figure 10 of three samples and follows the sequence of permeability. Pores with size belonging to interval II are probably potential ones determining permeability. Therefore, it is not the absolute amount of potential pores but the relative proportion of potential pores determining the permeability (Figure 10), in which potential pores means pores determining connectivity. Combined with the results of SEM and NMR  $T_2$ , pores fall in interval II in Figure 10 with radii ranging between nanometer to several microns, which are mostly clay-dominated pores identified by SEM. As noted above, we can conclude that these potential pores determining the permeability are clay-dominated pores. Therefore,

neither small pores with radii  $< 100$  nm (around peak 1 in NMR  $T_2$  distribution) nor large pores with radii  $> 5 \mu\text{m}$  (around peak 3 in NMR  $T_2$  distribution) control the permeability by analyzing the connectivity of the pores in various size ranges, but rather pores averaging approximately  $350 \pm X$  nm (around peak 2 in NMR  $T_2$  distribution) have sufficient connectivity to host and transmit hydrocarbons.

## 5. Conclusions

Three tight gas sandstone samples from the Linxing area, Ordos Basin, were collected to study the pore structure using various experimental techniques, including SEM, nitrogen adsorption, NMR  $T_2$ , and NMRC. The following conclusions are obtained.

- (1) Residual interparticle pores and clay-dominated pores are the two primary pore types for our target tight gas sandstone samples. Clay and quartz are the main minerals, accounting for almost excess 95% of the mineralogy content. The combined results of SEM and X-ray test show that pyrite is significantly distributed
- (2) The NMRC technique has a wide range of application to the pore structure characterization of tight gas sandstones, especially for pores with nanoscale radii. It can be a very promising method especially when referred to as a promising “roadmap” on how to interrogate tight formations, such as the tight gas sands or even shale
- (3) Porosity of tight gas sandstones is very low, exhibiting extremely poor correlations with the permeability. It is neither tiny pores nor large pores controlling the permeability of tight gas sandstone but relatively abundant pores, ranging around peak P2 of NMR  $T_2$  distribution ( $\sim 350$  nm). Pore types and their relative amounts of pores are critical factors determining the permeability. These potential pores determining the permeability of tight gas sandstones are associated with clay packets and folia (clay-dominated pores), which contribute a nontrivial volume to tight gas sandstones

## Data Availability

The data used to support the findings of this study are available from the corresponding author upon request.

## Conflicts of Interest

The authors declare that they have no conflicts of interest.

## Acknowledgments

The research is also supported by the Science Foundation of China University of Petroleum, Beijing (Grant No. 2462021XKBH007). In addition, DRC was supported by the US Department of Energy, Office of Science, Basic

Energy Sciences, Division of Chemical Sciences, Geosciences and Biosciences, Geosciences Program, under grant DE-SC0006878 to Ohio State University.

## References

- [1] B. Q. Dong, M. Meng, Z. S. Qiu, Z. H. Lu, Y. Zhang, and H. Y. Zhong, "Formation damage prevention using microemulsion in tight sandstone gas reservoir," *Journal of Petroleum Science and Engineering*, vol. 173, pp. 101–111, 2019.
- [2] F. Zhu, W. Hu, J. Cao, F. Sun, Y. Liu, and Z. Sun, "Micro/nano-scale pore structure and fractal characteristics of tight gas sandstone: a case study from the Yuanba area, Northeast Sichuan Basin, China," *Marine and Petroleum Geology*, vol. 98, pp. 116–132, 2018.
- [3] S. A. Holditch, "Tight gas sands," *Journal of Petroleum Technology*, vol. 58, no. 6, pp. 86–93, 2006.
- [4] J. Lai, G. W. Wang, Z. Y. Wang et al., "A review on pore structure characterization in tight sandstones," *Earth Science Reviews*, vol. 177, pp. 436–457, 2018.
- [5] H. Gao and H. A. Li, "Pore structure characterization, permeability evaluation and enhanced gas recovery techniques of tight gas sandstones," *Journal of Natural Gas Science and Engineering*, vol. 28, pp. 536–547, 2016.
- [6] C. N. Zou, R. K. Zhu, K. Y. Liu et al., "Tight gas sandstone reservoirs in China: characteristics and recognition criteria," *Journal of Petroleum Science and Engineering*, vol. 88–89, pp. 82–91, 2012.
- [7] M. Q. Chen, L. S. Cheng, X. K. Wang, C. H. Lyu, and R. Y. Cao, "Pore network modelling of fluid flow in tight formations considering boundary layer effect and media deformation," *Journal of Petroleum Science and Engineering*, vol. 180, pp. 643–659, 2019.
- [8] G. Desbois, J. L. Urai, P. A. Kukla, J. Konstanty, and C. Baerle, "High-resolution 3D fabric and porosity model in a tight gas sandstone reservoir: a new approach to investigate microstructures from mm- to nm-scale combining argon beam cross-sectioning and SEM imaging," *Journal of Petroleum Science and Engineering*, vol. 78, no. 2, pp. 243–257, 2011.
- [9] H. Wu, Y. L. Ji, R. Liu, C. L. Zhang, and S. Chen, "Insight into the pore structure of tight gas sandstones: a case study in the Ordos Basin, NW China," *Energy Fuels*, vol. 31, no. 12, pp. 13159–13178, 2017.
- [10] D. S. Xiao, S. F. Lu, J. X. Yang, L. C. Zhang, and B. Li, "Classifying multiscale pores and investigating their relationship with porosity and permeability in tight sandstone gas reservoirs," *Energy & Fuels*, vol. 31, no. 9, pp. 9188–9200, 2017.
- [11] F. P. Lai, Z. P. Li, T. T. Zhang, A. Q. Zhou, and B. Gong, "Characteristics of microscopic pore structure and its influence on spontaneous imbibition of tight gas reservoir in the Ordos Basin, China," *Journal of Petroleum Science and Engineering*, vol. 172, pp. 23–31, 2019.
- [12] S. Yu-jiang, H. Yang, M. Zhiqiang et al., "Comparisons of pore structure for unconventional tight gas," in *Coalbed Methane and Shale Gas Reservoirs In: SPE Asia Pacific Oil and Gas Conference and Exhibition*, Jakarta, Indonesia, 2013.
- [13] C. H. Lyu, Z. F. Ning, Q. Wang, and M. Q. Chen, "Application of NMRT2 to pore size distribution and movable fluid distribution in tight sandstones," *Energy & Fuels*, vol. 32, no. 2, pp. 1395–1405, 2018.
- [14] H. X. Huang, W. Sun, W. M. Ji et al., "Effects of pore-throat structure on gas permeability in the tight sandstone reservoirs of the Upper Triassic Yanchang formation in the Western Ordos Basin, China," *Journal of Petroleum Science and Engineering*, vol. 162, pp. 602–616, 2018.
- [15] X. H. Shao, X. Q. Pang, H. Li, and X. Zhang, "Fractal analysis of pore network in tight gas sandstones using NMR method: a case study from the Ordos Basin, China," *Energy Fuels*, vol. 31, no. 10, pp. 10358–10368, 2017.
- [16] X. H. Shao, X. Q. Pang, F. J. Jiang, L. L. Li, Y. Y. Huyan, and D. Y. Zheng, "Reservoir characterization of tight sandstones using nuclear magnetic resonance and incremental pressure mercury injection experiments: implication for tight sand gas reservoir quality," *Energy & Fuels*, vol. 31, no. 10, pp. 10420–10431, 2017.
- [17] A. Sakhaee-Pour and S. L. Bryant, "Effect of pore structure on the producibility of tight-gas sandstones," *AAPG Bulletin*, vol. 98, no. 4, pp. 663–694, 2014.
- [18] R. G. Loucks, R. M. Reed, S. C. Ruppel, and U. Hammes, "Spectrum of pore types and networks in mudrocks and a descriptive classification for matrix-related mudrock pores," *AAPG Bulletin*, vol. 96, no. 6, pp. 1071–1098, 2012.
- [19] S. Kolodzie Jr., "Analysis of pore throat size and use of the Waxman-Smits equation to determine OOIP in spindle field, Colorado," in *SPE Annual Technical Conference and Exhibition, Society of Petroleum Engineers*, p. 10, Dallas, Texas, 1980.
- [20] H. W. Zhao, Z. F. Ning, Q. Wang et al., "Petrophysical characterization of tight oil reservoirs using pressure-controlled porosimetry combined with rate-controlled porosimetry," *Fuel*, vol. 154, pp. 233–242, 2015.
- [21] R. Rezaee, A. Saeedi, and B. Clennell, "Tight gas sands permeability estimation from mercury injection capillary pressure and nuclear magnetic resonance data," *Journal of Petroleum Science and Engineering*, vol. 88–89, pp. 92–99, 2012.
- [22] M. Zou, C. Wei, Z. Huang, and S. Wei, "Porosity type analysis and permeability model for micro-trans-pores, meso-macropores and cleats of coal samples," *Journal of Natural Gas Science and Engineering*, vol. 27, pp. 776–784, 2015.
- [23] J. Zhang and Y. Hu, "Comparative evaluation of pore structure heterogeneity in low-permeability tight sandstones using different fractal models based on NMR technology: a case study of Benxi Formation in the Central Ordos Basin," *Energy & Fuels*, vol. 34, no. 11, pp. 13924–13942, 2020.
- [24] F. Tavenas, P. Jean, P. Leblond, and S. Leroueil, "The permeability of natural soft clays. Part II: permeability characteristics," *Canadian Geotechnical Journal*, vol. 20, no. 4, pp. 645–660, 1983.
- [25] M. Schmitt, C. P. Fernandes, F. G. Wolf, J. A. Bellini da Cunha Neto, C. P. Rahner, and V. S. Santiago dos Santos, "Characterization of Brazilian tight gas sandstones relating permeability and angstrom-to micron-scale pore structures," *Journal of Natural Gas Science and Engineering*, vol. 27, pp. 785–807, 2015.
- [26] L. M. Anovitz and D. R. Cole, "Characterization and analysis of porosity and pore structures," *Reviews in Mineralogy and Geochemistry*, vol. 80, no. 1, pp. 61–164, 2015.
- [27] B. Zhou, Q. Han, and P. Q. Yang, "Characterization of nanoporous systems in gas shales by low field NMR cryoporometry," *Energy & Fuels*, vol. 30, no. 11, pp. 9122–9131, 2016.
- [28] J. J. Zhang, C. Wei, W. Ju et al., "Stress sensitivity characterization and heterogeneous variation of the pore-fracture system

- in middle-high rank coals reservoir based on NMR experiments," *Fuel*, vol. 238, pp. 331–344, 2019.
- [29] C. H. Lyu, Z. F. Ning, M. Q. Chen, and Q. Wang, "Experimental study of boundary condition effects on spontaneous imbibition in tight sandstones," *Fuel*, vol. 235, pp. 374–383, 2019.
- [30] Q. Wang, C. H. Lyu, and D. R. Cole, "Effects of hydration on fractures and shale permeability under different confining pressures: an experimental study," *Journal of Petroleum Science and Engineering*, vol. 176, pp. 745–753, 2019.
- [31] P. Gane, C. J. Ridgway, E. Lehtinen et al., "Comparison of NMR cryoporometry, mercury intrusion porosimetry, and DSC thermoporosimetry in characterizing pore size distributions of compressed finely ground calcium carbonate structures," *Industrial and Engineering Chemistry Research*, vol. 43, no. 24, pp. 7920–7927, 2004.
- [32] A. Ostlund, T. Köhnke, L. Nordstierna, and M. Nydén, "NMR cryoporometry to study the fiber wall structure and the effect of drying," *Cellulose*, vol. 17, no. 2, pp. 321–328, 2010.
- [33] N. Gopinathan, B. Yang, J. P. Lowe, K. J. Edler, and S. P. Rigby, "NMR cryoporometry characterisation studies of the relation between drug release profile and pore structural evolution of polymeric nanoparticles," *International Journal of Pharmaceutics*, vol. 469, no. 1, pp. 146–158, 2014.
- [34] J. Y. Jehng, D. T. Sprague, and W. P. Halperin, "Pore structure of hydrating cement paste by magnetic resonance relaxation analysis and freezing," *Magnetic Resonance Imaging*, vol. 14, no. 7–8, pp. 785–791, 1996.
- [35] J. P. Korb, "NMR and nuclear spin relaxation of cement and concrete materials," *Current Opinion in Colloid & Interface Science*, vol. 14, no. 3, pp. 192–202, 2009.
- [36] P. Fantazzini, R. Viola, S. M. Alnaimi, and J. H. Strange, "Combined MR-relaxation and MR-cryoporometry in the study of bone microstructure," *Magnetic Resonance Imaging*, vol. 19, no. 3–4, pp. 481–484, 2001.
- [37] V. M. Gun'ko, V. V. Turov, A. P. Shpilko et al., "Relationships between characteristics of interfacial water and human bone tissues," *Colloids and Surfaces B: Biointerfaces*, vol. 53, no. 1, pp. 29–36, 2006.
- [38] Y. X. Zhao, Y. F. Sun, S. M. Liu, K. Wang, and Y. D. Jiang, "Pore structure characterization of coal by NMR cryoporometry," *Fuel*, vol. 190, pp. 359–369, 2017.
- [39] T. T. Yin, D. M. Liu, Y. D. Cai, Y. F. Zhou, and Y. B. Yao, "Size distribution and fractal characteristics of coal pores through nuclear magnetic resonance cryoporometry," *Energy & Fuels*, vol. 31, no. 8, pp. 7746–7757, 2017.
- [40] B. Liu, S. P. Yao, W. X. Hu, J. Cao, and D. L. Xie, "Application of nuclear magnetic resonance cryoporometry in unconventional reservoir rocks," *Acta Petrologica Sinica*, vol. 38, no. 12, pp. 1401–1410, 2017.
- [41] Z. P. Wang and T. Wang, "A brief introduction to the principle and application of nuclear magnetic resonance cryoporometry," *Materials Reports*, vol. 27, no. 1, pp. 129–133, 2013.
- [42] Q. Zhang, Y. H. Dong, S. Q. Tong, X. Li, and L. H. Wang, "Nuclear magnetic resonance cryoporometry as a tool to measure pore size distribution of shale rock," *Chinese Science Bulletin*, vol. 61, no. 21, pp. 2387–2394, 2016.
- [43] M. Firouzi, E. C. Rupp, C. W. Liu, and J. Wilcox, "Molecular simulation and experimental characterization of the nanoporous structures of coal and gas shale," *International Journal of Coal Geology*, vol. 121, pp. 123–128, 2014.
- [44] J. B. W. Webber, "The dimensional term in the Gibbs-Thomson equation, describing the behaviour of liquids in porous media, is being investigated by NMR relaxation, novel protocol NMR cryoporometry, neutron scattering and ab initio QM-MD simulation," *Magnetic Resonance Imaging*, vol. 25, no. 4, pp. 589–590, 2007.
- [45] J. C. Dore, J. B. W. Webber, and J. H. Strange, "Characterisation of porous solids using small-angle scattering and NMR cryoporometry," *Colloids and Surfaces A: Physicochemical and Engineering Aspects*, vol. 241, no. 1–3, pp. 191–200, 2004.
- [46] O. V. Petrov and I. Furó, "NMR cryoporometry: principles, applications and potential," *Progress in Nuclear Magnetic Resonance Spectroscopy*, vol. 54, no. 2, pp. 97–122, 2009.
- [47] K. S. W. Sing, "Reporting physisorption data for gas/solid systems with special reference to the determination of surface area and porosity (recommendations 1984)," *Pure and Applied Chemistry*, vol. 57, no. 4, pp. 603–619, 1985.
- [48] F. Yang, Z. F. Ning, Q. Wang, R. Zhang, and B. M. Krooss, "Pore structure characteristics of lower Silurian shales in the southern Sichuan Basin, China: insights to pore development and gas storage mechanism," *International Journal of Coal Geology*, vol. 156, pp. 12–24, 2016.
- [49] J. Rouquerol, D. Avnir, C. W. Fairbridge et al., "Recommendations for the characterization of porous solids (technical report)," *Pure and Applied Chemistry*, vol. 66, no. 8, pp. 1739–1758, 1994.